НАУЧНО-ТЕХНИЧЕСКИЙ ВЕСТНИК ИНФОРМАЦИОННЫХ ТЕХНОЛОГИЙ, МЕХАНИКИ И ОПТИКИ
январь–февраль 2026 Том 26 № 1 http://ntv.ifmo.ru/
SCIENTIFIC AND TECHNICAL JOURNAL OF INFORMATION TECHNOLOGIES, MECHANICS AND OPTICS
January–February 2026 Vol. 26 No 1 http://ntv.ifmo.ru/en/
ISSN 2226-1494 (print) ISSN 2500-0373 (online)

doi: 10.17586/2226-1494-2026-26-1-15-25

Defocus-resolved construction of process windows in nanosecond laser irradiation of oxidized silicon

Huynh Cong Tu✉

Quy Nhon University, Quy Nhon, 55131, Viet Nam

huynhcongtu@qnu.edu.vn✉, https://orcid.org/0000-0002-5184-8242

Abstract

We present a defocus-dependent, quantitatively validated framework for nanosecond fiber-laser irradiation of thermally oxidized silicon. By systematically varying the beam defocus, the on-axis peak power density i and spot diameter d are correlated with distinct surface morphologies on SiO_2 (150 nm)/Si (111). Controlled scanning experiments made with nanosecond fiber laser (IRE-Polyus ILI-1-50, wave length $\lambda = 1062$ nm, pulse width $\tau \approx 120$ ns, Pulse Repetition Frequency 50 kHz, and scan velocity $v = 100$ mm·s^{-1}) reveal a continuous morphological sequence — wrinkling, blistering, and premelting — governed by thermo-mechanical stress and interfacial adhesion. Surface features were quantified using two-dimensional Fourier analysis for wrinkle wavelength ($\lambda \approx 8$–10 μm) and automated image segmentation for blister size distributions (1–3 μm). Point-exposure measurements yield a blister-onset energy of 0.09 J, corresponding to a per-pulse fluence of 0.17 J·cm^{-2}. Logistic regression with 95 % bootstrap confidence intervals with bootstrap replications $B = 2000$ defines the wrinkle-to-premelting transition, producing a statistically bounded (I, d) phase diagram. Control experiments confirm that both dynamic scanning and the oxide cap are indispensable: point irradiation on SiO_2/Si produces only shallow ⟨110⟩ slip lines from substrate relaxation, while bare Si remains featureless under identical conditions. Hydrofluoric (HF) etching verifies that the observed blisters are true interfacial delaminations. This framework extends classical buckling–delamination mechanics to cyclic nanosecond heating and provides predictive guidelines for precision, sub-melting laser microfabrication of dielectric–semiconductor systems.

Keywords

laser processing, process window, oxidized silicon, morphological transitions, statistical modeling, surface engineering

Acknowledgements

This work was supported by Quy Nhon University through an institutional Science-and-Technology Project.
The author sincerely thanks colleagues and mentors for constructive discussions and feedback.

For citation: Tu H.C. Defocus-resolved construction of process windows in nanosecond laser irradiation of oxidized silicon. *Scientific and Technical Journal of Information Technologies, Mechanics and Optics*, 2026, vol. 26, no. 1, pp. 15–25. doi: 10.17586/2226-1494-2026-26-1-15-25

УДК 621.373.8

Построение технологических окон с дефокусированным разрешением при наносекундном лазерном облучении окисленного кремния

Хуинь Конг Ту✉

Университет Куинён, Куинён, 55131, Вьетнам

huynhcongtu@qnu.edu.vn✉, https://orcid.org/0000-0002-5184-8242

Аннотация

Разработана дефокусно-зависимая, количественно подтвержденная методика облучения термически окисленного кремния (SiO_2) волоконным лазером с наносекундной длительностью импульсов. Систематическое изменение дефокуса пучка позволило установить корреляцию между пиковой осевой плотностью мощности I и диаметром пятна d с различными морфологическими состояниями поверхности структуры пленки SiO_2 толщиной 150 нм на поверхности кремниевой пластины, ориентированной в кристаллографической плоскости (111). В контролируемых экспериментах сканирования (длина волны $\lambda = 1062$ нм, ширина импульса $\tau \approx 120$ нс, частота

повторения импульсов 50 кГц, скорость сканирования 100 мм·с$^{-1}$) наблюдалась непрерывная последовательность морфологических превращений: сморщивание, пузырение и предплавление, — обусловленных термомеханическими напряжениями и межфазной адгезией. Параметры поверхности определялись методом двумерного преобразования Фурье (длина волны складок 8–10 мкм) и автоматической сегментацией изображений (распределения размеров пузырей 1–3 мкм). При точечном воздействии установлена энергия начала пузырения 0,09 Дж, соответствующая флюенсу одного импульса 0,17 Дж·см$^{-2}$. С использованием логистической регрессии с 95 %-ными бутстреп-доверительными интервалами (B = 2000) определен переход от стадии сморщивания к предплавлению и построена статистически ограниченная фазовая диаграмма в координатах (I, d). Контрольные эксперименты показали, что динамическое сканирование и наличие оксидной пленки являются необходимыми условиями: при точечном облучении SiO_2/Si формируются неглубокие скользящие линии ⟨110⟩ вследствие релаксации подложки, а поверхность чистого Si остается неизменной при тех же параметрах. Травление в плавиковой кислоте подтвердило, что наблюдаемые пузыри представляют собой истинные межфазные деламинации. Предложенный подход распространяет классическую механику вспучивания–деламинации на режим циклического наносекундного нагрева и формирует основу для прогнозируемой высокоточной подплавляющей лазерной микрофабрикации диэлектрическо-полупроводниковых структур.

Ключевые слова

лазерная обработка, технологическое окно, окисленный кремний, морфологические переходы, статистическое моделирование, инженерия поверхности

Благодарности

Исследование выполнено при поддержке Университета Куинён (Вьетнам) в рамках институционального проекта в области науки и технологий.

Автор выражает искреннюю благодарность коллегам и наставникам за конструктивные обсуждения, полезные советы и ценные замечания.

Ссылка для цитирования: Ту Х.К. Построение технологических окон с дефокусированным разрешением при наносекундном лазерном облучении окисленного кремния // Научно-технический вестник информационных технологий, механики и оптики. 2026. Т. 26, № 1. С. 15–25 (на англ. яз.). doi: 10.17586/2226-1494-2026-26-1-15-25

Introduction

Laser conditioning of thermally oxidized silicon is fundamental to microelectronic fabrication and precision metrology where sub-melting surface modification enables defect control and improved device reliability [1–3]. Despite extensive research on laser-induced structuring of SiO_2/Si and ultrafast Laser-Induced Periodic Surface Structure (LIPSS) formation [4–6], the quantitative relationship between optical defocus — hence local energy density — and morphological transitions under scanned nanosecond irradiation remains largely unresolved. This gap limits predictive control and the ability to define reliable, high-throughput process windows for oxide-semiconductor systems.

Under nanosecond laser irradiation at a near-infrared wavelength around 1 μm, where silicon exhibits strong subsurface absorption and the oxide remains largely transparent, interfacial thermoelastic loading dominates the sub-melting regime. It is hypothesized that defocus governs a continuous transition from elastic wrinkling to blistering and localized premelting through an energy-density scaling proportional to $P/(Vd^2)$, where P is laser power, V is scan velocity, and d is spot diameter. This scaling reflects the balance between optical energy delivery and thermal diffusion, capturing how stress accumulation and dissipation drive surface instability. Wrinkling and blistering originate from the competition between compressive stress and interfacial adhesion at the SiO_2/Si boundary — consistent with cohesive-zone buckling and delamination mechanics — whereas premelting arises once local fluence exceeds the softening threshold. This interpretation is supported by evidence of gigapascal-level stresses and thermal softening in SiO_2 [7], cohesive-zone modeling of buckle geometry [8], direct nonosecond scale blister formation [9], stress-induced thermoplastic deformation in Si [10], and controlled interfacial melting in the nanosecond range transmission welding [11].

Recent studies highlight defocus as an active control parameter that redistributes laser energy and modifies morphology in additive manufacturing [12], thin-film deposition [11], and oxide removal [13]. However, these effects remain qualitative for nanosecond heating of oxide-coated silicon. Unlike polarization-locked ultrafast LIPSS [4, 14], nanosecond pulses couple absorption, heat diffusion, and stress relaxation, producing complex stress-driven morphologies including wrinkling, blistering, and local melting [15]. Earlier nanosecond studies of SiO_2/Si were descriptive and fluence-based [16], without quantitative phase mapping.

Here, there established a defocus-resolved, statistically validated morphology map that links the on-axis peak intensity I and spot diameter d to wrinkling, blistering, and premelting regimes. Combining calibrated thermography, quantitative surface metrology, and logistic modeling with bootstrap confidence 95 %, with bootstrap replications B = 2000, we delineate transition boundaries in the (I, d) space. This framework extends classical buckling-delamination mechanics into the cyclic, nanosecond heating regime and provides predictive design rules for stable, sub-melting laser processing of SiO_2/Si and related thin-film systems.

Materials and Methods

Substrates

Single-crystal Si(111) (KDB-10), front side polished and backside roughened. A thermally grown SiO_2 cap with a thickness of 150 nm was used.

Laser and optics

Experiments employed a nanosecond fiber laser (IRE-Polyus ILI-1-50, with wave length $\lambda = 1062$ nm, pulse width $\tau = 120$ ns, Pulse Repetition Frequency (PRF) = = 50 kHz, average power $P_{max} = 50$ W) coupled to an *f*-theta scan lens (lens focus $f = 184.4$ mm). The beam operated in the TEM_{00} mode ($M^2 \approx 1.15$) and impinged normally on the wafer. Ten defocus settings (Δz = = 0–1.6 mm) produced spot diameters from 139 ± 5 μm to 519 ± 15 μm at the sample plane, as summarized in Table 1.

Central temperature profiles in Fig. 1, *a*, along the beam axis, were obtained using a Forward Looking Infrared (FLIR) thermography system. These profiles show the peak surface temperature T_{max} for three defocused beam diameters (d = 139, 333, and 519 μm). The inset presents a representative thermal image captured by the FLIR system and used to extract the temperature cross-section. Fig. 1, *b–d* displays 3D surface maps reconstructed from the same dataset, revealing a progressive decrease in both peak temperature and thermal gradient with increasing defocus. Beam diameters were determined from the $1/e^2$ width of the thermal profiles, consistent with Gaussian fitting.

Table 1. Measured and calculated beam diameters at different defocus positions

Δz, mm	Measured d, μm	Calculated $d(z)$, μm
0.00 (focus)	139 ± 5	138
+0.20	180 ± 6	177
+0.40	230 ± 7	225
+0.60	275 ± 8	267
+0.80	315 ± 9	308
+1.00	360 ± 10	349
+1.20	405 ± 12	394
+1.35	460 ± 13	452
+1.50	495 ± 14	498
+1.60	519 ± 15	512

Beam geometry at the processing plane was quantified using an infrared thermal imaging system (FLIR thermal camera, 3–5 μm spectral range, 12 μs integration time). The camera recorded transient temperature fields produced by

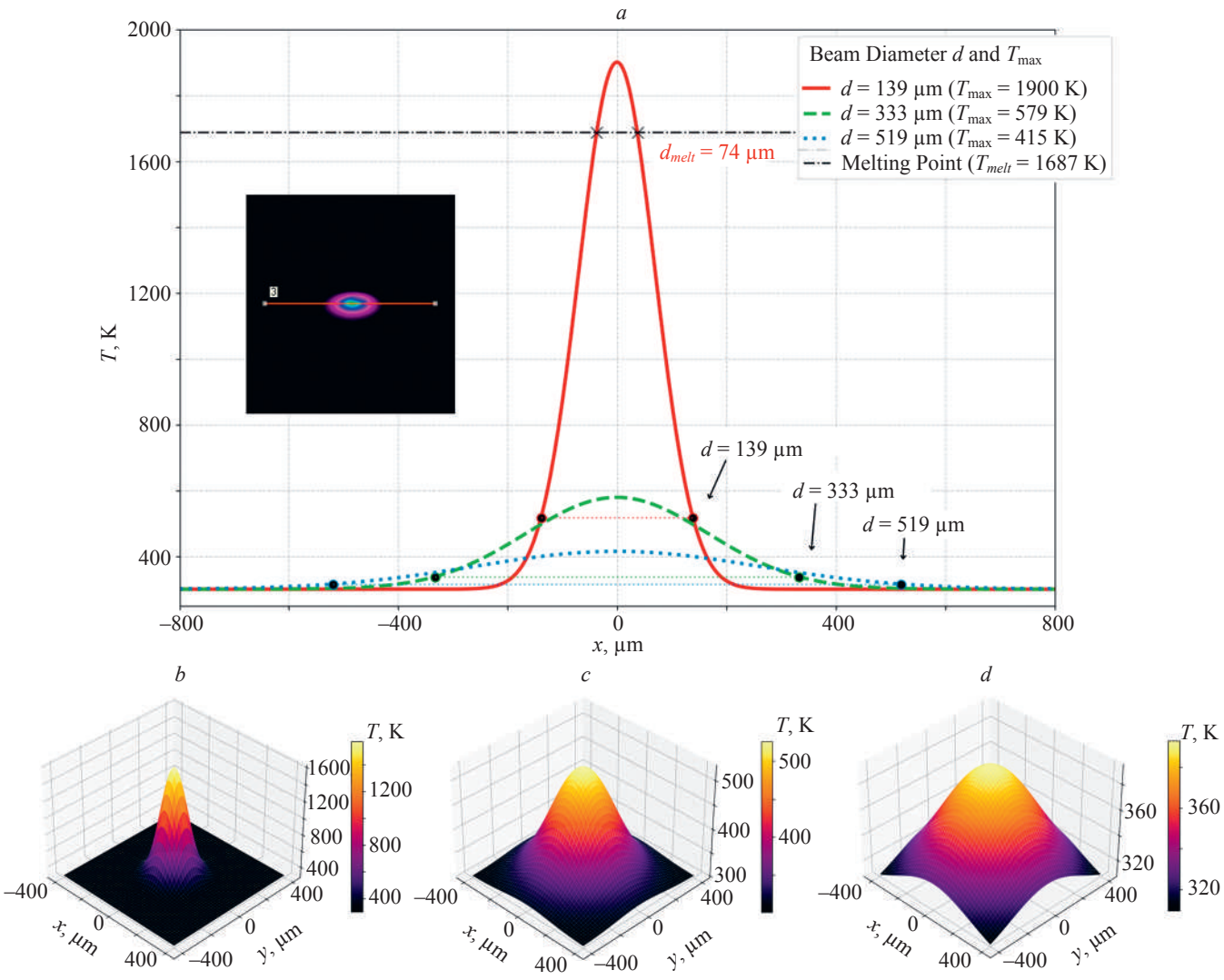

Fig. 1. Temperature (T) field and beam-profile calibration for different defocus settings: central temperature profiles along the beam axis (*a*) and 3D surface maps (*b–d*)

single laser shots on a matte SiO_2/Si surface. The emissivity of the surface was calibrated to 0.80 using a thermocouple reference. The captured thermal maps exhibited circular symmetry and a Gaussian-like temperature distribution (Fig. 1), confirming that the absorbed energy followed a Gaussian spatial envelope. Line profiles across the hot-spot center (Fig. 1, *a*) were fitted to Gaussian curves, and the $1/e^2$ width was taken as the effective beam diameter d.

Defocus variation (Δz) was related to the beam diameter by Gaussian-beam propagation theory:

$$d(z) = 2w_0\sqrt{1 + \left(\frac{\Delta z}{z_R}\right)^2},\ z_R = \frac{\pi w_0^2}{\lambda},$$

where w_0 is the beam waist radius and z_R the Rayleigh length. For $\lambda = 1062$ nm and $w_0 = 69.5$ μm, $z_R \approx 0.69$ mm. The measured and predicted diameters agreed within ±5 % (Table 1), validating both the optical alignment and the thermal-imaging calibration.

Peak power density was evaluated as $I = 4P/(\pi d^2)$ where P is the average laser power (W) and d the $1/e^2$ diameter (cm). The energy-density scaling parameter $P/(Vd^2)$ with scan velocity V (cm·s^{-1}), represents the rate of energy delivery per unit area and governs the defocus–morphology transition.

Scan and point-exposure protocols

Laser irradiation was conducted using a galvanometer-based scanner at a constant velocity of $v = 100$ mm·s^{-1}. For each defocus setting, the peak power density I at the track center was set by the average power and measured d. Stationary exposures (no scanning) were also performed using the largest spot ($d \approx 519$ μm) at four intensity levels to examine localized blister formation. The dwell time during scanning was approximated by $t_{dwell} \approx d/v$ and the pulse count $N = PRF \cdot t_{dwell}$. The corresponding dwell times and pulse counts are summarized in Table 2.

Image acquisition and analysis

Laser-processed surfaces were inspected by bright-field Optical Microscopy with in-frame scale calibration. Optical imaging was performed using a ZEISS Axio Imager microscope with a 50× objective (Numerical Aperture, NA = 0.75), providing a lateral resolution of 0.4 μm and a calibrated pixel size of 0.15 μm. Atomic Force Microscopy (AFM) measurements were carried out in tapping mode on a Nanosurf NanoEducator system, achieving 10 nm lateral and 0.1 nm vertical resolution. Wrinkle quantification used square Regions of Interest (ROI, 1024 × 1024 px) extracted from wrinkle-rich segments. Images were mean-subtracted, linearly detrended, and Hann-windowed before applying a two-dimensional Fast Fourier Transform (2D FFT). The amplitude spectra were converted to spatial frequency (μm^{-1}) using microscope calibration. The dominant wrinkle spacing was obtained as

$$\lambda = \frac{2\pi}{k^*},$$

where k^* is the peak of the azimuthally averaged spectrum; the normalized width $\Delta k/k^*$ is quantified periodicity sharpness.

Blister statistics were extracted from point-exposure images via global Otsu thresholding [17], followed by morphological opening (a disk radius of 2 px). Connected components touching image borders were excluded, and small artifacts ($A < 0.50$ μm^2) removed. Equivalent diameters were computed as

$$D_{\text{eq}} = 2\sqrt{\frac{A}{\pi}}.$$

Histograms (24 bins spanning 0.2–8 μm) were generated for each exposure level; descriptive statistics are reported later. Oxide coloration was verified by comparing observed interference colors with standard SiO_2 thickness charts [18].

To delineate the morphological regime boundaries, a logistic regression model was fitted in the lg I, lg d space, treating each observation as a binary outcome (wrinkling is equal to 0, premelting is equal to 1). The probability of premelting follows

$$p = \frac{1}{1 + \exp[-(\beta_0 + \beta_2 \lg I + \beta_2 \lg d)]}.$$

Here, β_0 is the intercept representing the baseline tendency for premelting, β_1 quantifies the sensitivity of the transition to laser intensity I, and β_2 captures the

Table 2. Scanning and point-exposure parameters

Defocus condition	Spot diameter d, μm	Dwell time $t_{dwell} = d/v$, ms	Pulses per spot $N = PRF \cdot t_{dwell}$	Peak power density I, $W \cdot cm^{-2}$	Exposure mode
0.00 (focus)	139	1.39	70	3.31×10^5	Scan
+0.20	180	1.80	90	1.97×10^5	Scan
+0.40	230	2.30	115	1.20×10^5	Scan
+0.60	275	2.75	138	7.89×10^4	Scan
+0.80	315	3.15	158	5.08×10^4	Scan
+1.00	360	3.60	180	3.27×10^4	Scan
+1.20	405	4.05	203	2.43×10^4	Scan
+1.35	460	4.60	230	1.81×10^4	Scan
+1.50	495	4.95	248	1.46×10^4	Point/Scan
+1.60	519	5.19	260	1.26×10^4	Point/Scan

compensating effect of the spot diameter d on thermal and mechanical loading. The transition contour ($p = 0.5$) defines the boundary between wrinkling and premelting, given by

$$\lg I = -\frac{\beta_0}{\beta_1} - \frac{\beta_2}{\beta_1}\lg d. \quad (1)$$

Model coefficients were obtained using Iteratively Reweighted Least Squares. Uncertainty was quantified via non-parametric bootstrap resampling ($B = 2000$); the 2.5th–97.5th percentile envelope defines the 95 % confidence band detailed in the Quantitative process mapping section. This statistical framework provides a reproducible, quantitative link between experimental morphologies and energy-density scaling, enabling predictive determination of the wrinkle, blister, and premelting regimes.

Derived metrics

To facilitate comparison across defocus conditions, the derived laser-scan parameters are summarized in Table 3. $PRF = 50$ kHz and a scan speed of $v = 100$ mm·s^{-1} yield a pulse pitch of 500 mm^{-1} (approximately 2 μm). Lineic energy ($P_{avg}/v = 0.5$ J·mm^{-1}) and line fluence ($F_{line} = (P_{avg}/v)/d$) were computed for $P_{avg} = 50$ W. These average-power values are given for context only; regime boundaries established in our subsequent phase-diagram analysis were derived from the peak intensity I, spot size d, and point-exposure nucleation energy E_{nuc}. Defocus thus modulates both spatial (d) and temporal (t_{dwell}, N) exposure, governing the balance between energy accumulation, stress buildup, and localized melting.

Results and Discussion

Overview and novelty

Laser-induced deformation of oxide-semiconductor bilayers has long been reported through thermally driven wrinkling, implantation-induced blistering, and surface melting. However, most previous works relied on average fluence as a process descriptor and treated each instability separately, leaving unresolved how peak intensity and scanning dynamics together control the transition between elastic buckling, interfacial delamination, and thermal softening.

The present study establishes a defocus-resolved process map that quantitatively links the on-axis peak power density and the spot diameter d to distinct morphological regimes on SiO_2/Si (Table 4). Combining calibrated infrared thermography, quantitative surface metrology, and HF-etch validation, this work provides the first statistically bounded phase diagram for nanosecond scanning irradiation of SiO_2/Si. The approach converts empirical morphology observations into a predictive, physics-based framework, bridging optical energy deposition with thin-film mechanics.

Morphological evolution with defocus

The evolution of SiO_2/Si morphologies under nanosecond scanning is shown in Fig. 2, where defocus serves as the single control parameter regulating both peak intensity and pulse overlap. The spot diameter varied from approximately 139 μm to 519 μm, corresponding to 70–260 overlapping pulses per spot. At small $d = 139$ μm ($I \approx 1.6 \cdot 10^5$ W·cm^{-2}), the oxide film exhibits periodic

Table 3. Derived exposure parameters for different defocus settings

Δz, mm	Spot diameter d, μm	Dwell time t_{dwell}, ms	Pulses per spot N	Lineic energy P_{avg}/v, J·mm^{-1}	Line fluence F_{line}, J·mm^{-2}	Line fluence, J·cm^{-2}
0.00 (focus)	139	1.39	70	0.50	3.60	360
+0.20	180	1.80	90	0.50	2.78	278
+0.40	230	2.30	115	0.50	2.17	217
+0.60	275	2.75	138	0.50	1.82	182
+0.80	315	3.15	158	0.50	1.59	159
+1.00	360	3.60	180	0.50	1.39	139
+1.20	405	4.05	203	0.50	1.23	123
+1.35	460	4.60	230	0.50	1.09	109
+1.50	495	4.95	248	0.50	1.01	101
+1.60	519	5.19	260	0.50	0.963	96.3

Table 4. Comparison with previous studies

Feature	This work	Ref [16]	Ref [19]
Parameter	Defocus Δz	Fluence	Fluence
Morphology map	Quantitative (defocus–intensity phase diagram)	Qualitative (descriptive morphology)	Single-point analysis
Statistics	Logistic regression + Bootstrap (confidence interval is 95 %)	None	None
Mechanism	Cyclic thermo-mechanical coupling + hydrofluoric (HF) acid validation	Descriptive mechanism of micro structuring	Threshold-based damage
Process window	Defined in (I, d) space	None	None

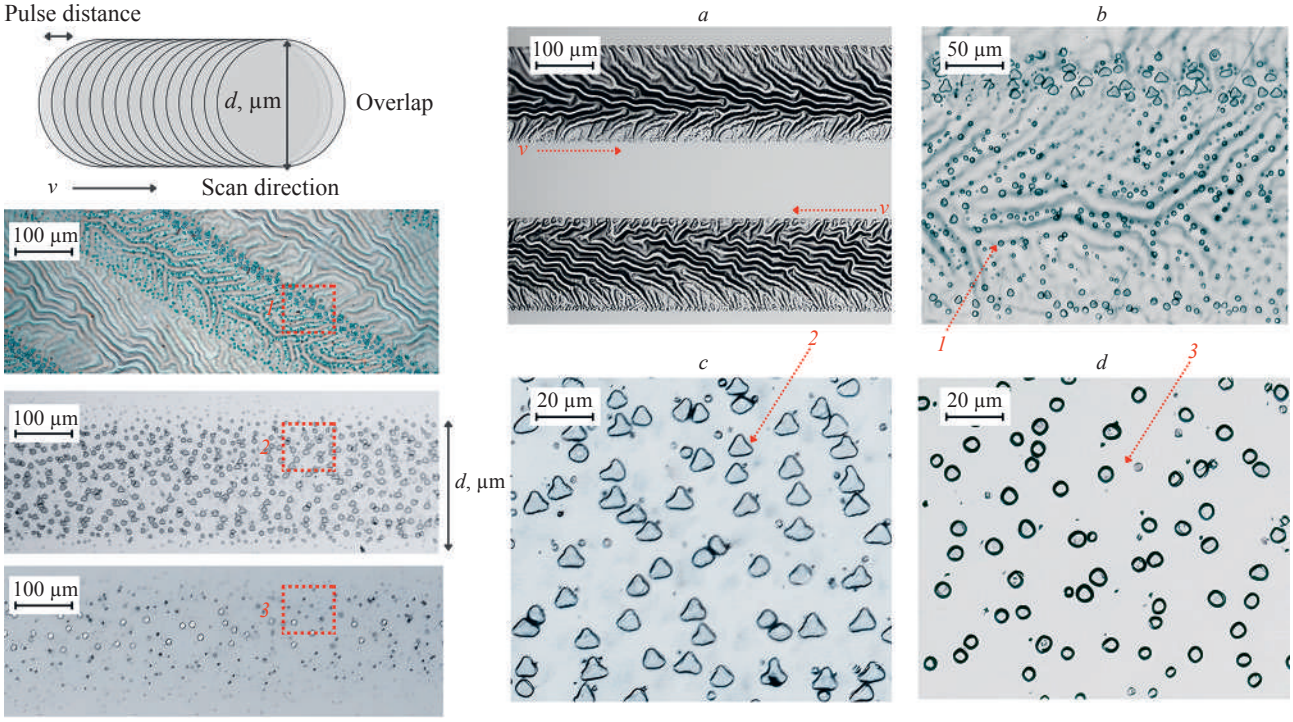

Fig. 2. Defocus-dependent morphological evolution of SiO_2/Si under nanosecond laser scanning: schematic of pulse overlap during scanning (*a*), where *d* denotes the laser spot diameter and *v* denotes the scan velocity direction; optical micrographs showing transitions from wrinkling at small defocus (d = 139 μm), to the coexistence of wrinkles and blisters at intermediate defocus (d = 333 μm), and finally to isolated blisters at large defocus (d = 519 μm) (*b–d*).

Numeration: *1* — wrinkled surface/wrinkle ridges; *2* — triangular blisters; *3* — circular/annular blisters observed under large defocus

wrinkles oriented perpendicular to the scan direction. The observed wrinkle wavelength $\lambda \approx 8$–10 μm, follows the elastic buckling relation $\lambda = 2\pi t(E_f/3E_s)^{1/3}$, where t = 150 nm is the film thickness, and $E_f \approx 70$ GPa and $E_s \approx 170$ GPa denote the Young's moduli of the oxide film and Si substrate, respectively [20]. At intermediate $d \approx 250$–350 μm ($I \approx (3–8)\cdot 10^4$ W·cm^{-2}), isolated triangular or circular blisters nucleate atop the wrinkles, with median equivalent diameter 2.6 ± 0.7 μm, indicating localized interfacial delamination. Blisters nucleate preferentially in the central region of the laser spot $r < 0.7d$, where the local intensity exceeds the delamination threshold I_{nuc}. The areal density gradually decreases toward the beam periphery, consistent with the Gaussian spatial intensity distribution of the laser (Fig. 1). At large $d \approx 500$ μm ($I \approx 4.5\cdot 10^3$ W·cm^{-2}), the surface becomes smooth and wrinkle-free, as the elastic energy falls below the buckling threshold. The continuous morphological sequence – wrinkling → blistering → → premelting — demonstrates that defocus continuously tunes the competition between stress accumulation and thermal relaxation, a behavior not previously quantified for nanosecond laser scanning.

Mode and material controls

Control experiments clarify the distinct roles of scanning dynamics and the oxide cap (Fig. 3). Under stationary point irradiation (no scanning) at d = 519 μm and $I \approx 4.5$W·cm^{-2}, the surface remains mostly smooth except for faint cross-hatched slip lines along ⟨110⟩ directions. AFM mapping reveals shallow ridges of approximately 20 nm amplitude, characteristic of thermally activated plastic slip in silicon rather than interfacial deformation.

When the oxide layer is removed (bare Si), neither scanning nor stationary exposure produces any surface features. The SiO_2 film thus provides both the bending stiffness required for buckling and the interfacial confinement for delamination, while the moving beam produces cyclic thermal gradients that accumulate compressive stress. These controls confirm that wrinkling and blistering are oxide-mediated instabilities unique to scanning, while the slip-line structures in point exposure correspond to substrate relaxation. This resolves prior ambiguities where slip and blister morphologies were conflated.

Verification of interfacial delamination

The interfacial origin of the blisters is validated through HF etching (Fig. 4). Before etching, the features appear as dome-like protrusions with optical interference coloration; after etching, these domes collapse into pits, confirming that they are hollow oxide membranes delaminated from the substrate rather than regions of oxidation or melting. No contrast is observed outside the blistered zones, verifying that the surrounding oxide remains intact. This chemical verification provides direct proof of interfacial decohesion as the mechanism of blistering. Similar cavities have been reported in H-implanted or thermally stressed SiO_2/Si systems [19], but here the phenomenon arises solely from laser-induced thermo-mechanical stress, without ion implantation or plasma assistance. The result broadens the understanding of high-rate interfacial delamination.

Quantitative process mapping

All observations are consolidated in Fig. 5, which presents the defocus–intensity (I, d) phase diagram

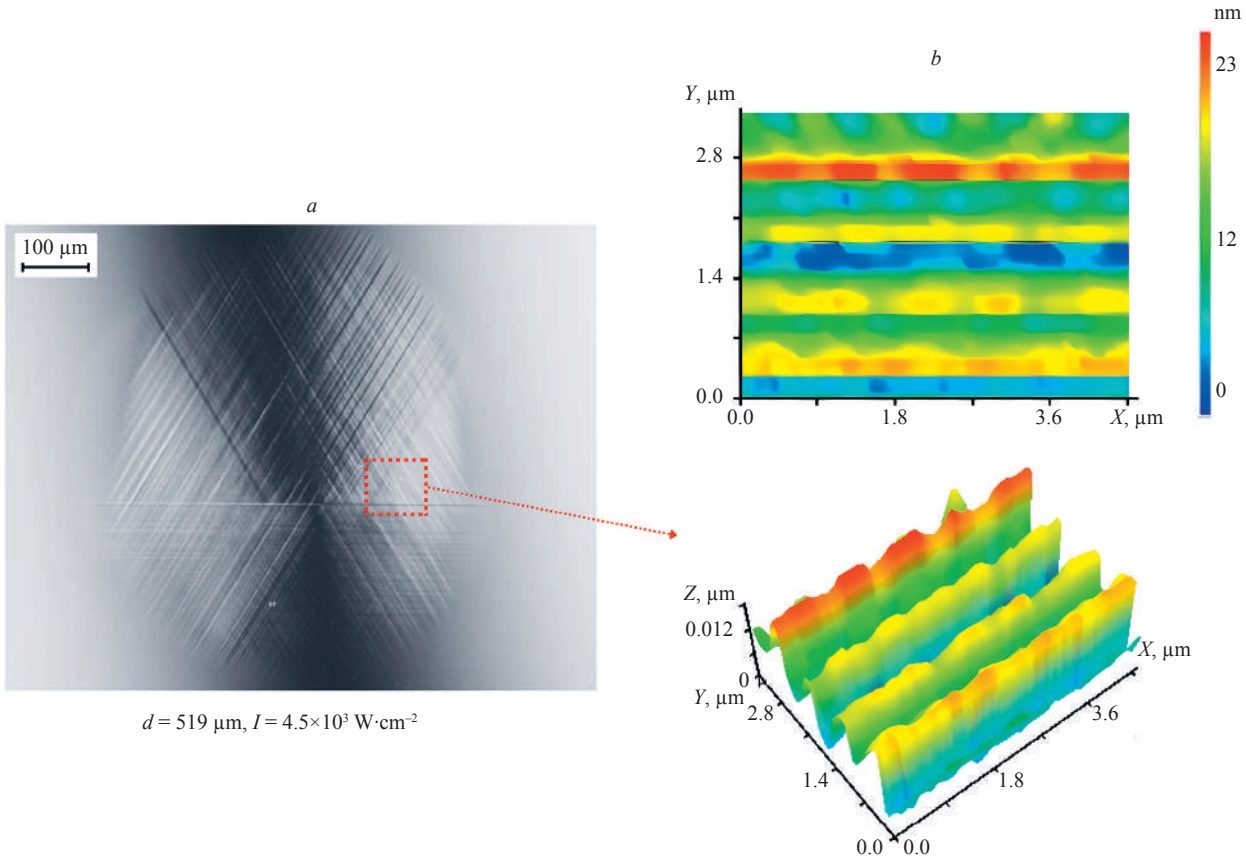

Fig. 3. Control experiments revealing the role of oxide and scan dynamics: is stationary point irradiation on SiO_2/Si showing cross-hatched slip lines (*a*); is AFM mapping confirming shallow ridges (20 nm) (*b*), where the 0–2 nm vertical color scale denotes the AFM surface height (topographic elevation), *h* (nm); together demonstrating substrate plastic slip. Absence of features on bare Si under identical conditions confirms that wrinkling/blistering require both the SiO_2 film and scanning-induced stress gradients

distinguishing three domains: elastic wrinkling, interfacial blistering, and premelting. The wrinkle-to-premelting boundary follows a logistic fit in (lg *I*, lg *d*) space, with a 95 % bootstrap confidence band ($B = 2000$). The phase diagram (Fig. 5) was validated using $N = 45$ independent scan tracks acquired across ten defocus settings (Table 2), with three to five replicates per condition. The logistic regression model correctly classified 42 out of 45 experimental points, corresponding to a prediction accuracy of 92 %. This high consistency confirms the statistical robustness of the derived wrinkle-premelting boundary and supports the physical validity of the (*I*, *d*) process map. The

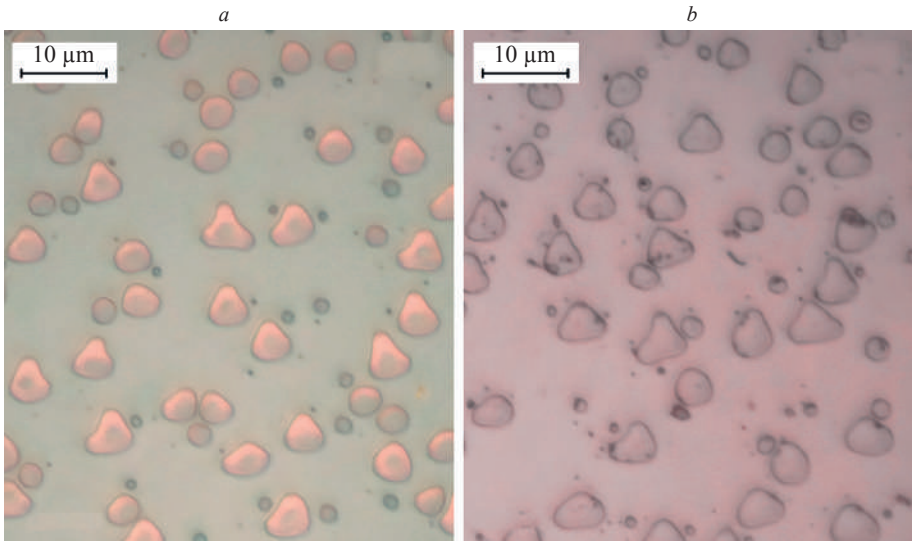

Fig. 4. HF-etch verification of interfacial delamination: before etching, dome-like blisters with interference coloration (*a*); after etching, blisters collapse into pits, proving that they are hollow, delaminated SiO_2 membranes rather than melted or oxidized regions (*b*)

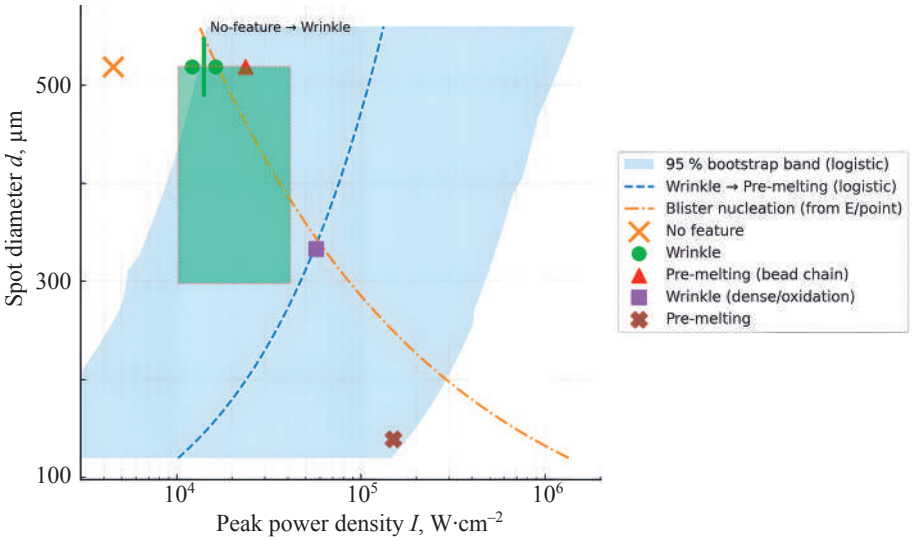

Fig. 5. Defocus–intensity (I, d) phase diagram showing the experimentally determined transitions among wrinkling, blistering, and premelting. The dashed curve represents the logistic boundary (95 % bootstrap band, $B = 2000$), and the dash–dot curve denotes the blister-nucleation threshold. Shaded green region ($10^4 < I < 4{\cdot}10^4$ W·cm^{-2}, $300 < d < 520$ μm) represents the stable wrinkling window suitable for controlled submelting surface texturing

blister-nucleation boundary is derived from the classical energy-balance criterion for interfacial delamination:

$$\frac{\sigma_c^2 h}{2E_f} = \Gamma_{int}, \qquad (2)$$

where σ_c is critical compressive stress in the oxide film (Pa); h = 150 nm is SiO_2 film thickness; E_f = 70 GPa is Young's modulus of the SiO_2 film; $\Gamma_{int} \approx$ J·m^{-2} is interfacial adhesion (fracture) energy between SiO_2 and Si. Substituting these values into Eq. (2) yields a critical stress of $\sigma_c \approx 0.9$ GPa and a corresponding nucleation intensity of $I_{nuc} \approx 4{\cdot}10^4$ W·cm^{-2}, consistent with the experimental blister onset near a spot diameter of $d \approx 333$ μm. The transition from a featureless surface to wrinkle formation occurs at a peak intensity of approximately $I \approx 1.4{\cdot}10^4$ W·cm^{-2} for a spot diameter of d = 519 μm (Table 5). Together, these boundaries define a stable wrinkling window bounded below by insufficient stress and above by delamination or melting. Unlike earlier fluence-based maps [21], this quantitatively grounded diagram relates observable morphology to measurable physical parameters (I, d, v), providing a predictive basis for sub-melting laser processing [22].

The process window is governed by four physical constraints. At low intensity ($I < 10^4$ W·cm^{-2}), the thermal stress remains below the critical value ($\sigma < \sigma_c$) and no buckling occurs.

At high intensity ($I < 10^5$ W·cm^{-2}), the local temperature exceeds the softening point of SiO_2 ($T > T_{melt}$). The blister-nucleation threshold appears near $I \approx 4{\cdot}10^4$ W·cm^{-2} when the energy-release rate G surpasses the adhesion energy Γ, causing interfacial delamination. In addition, the spot size d modulates stress accumulation: small d leads to higher pulse overlap and greater residual stress, whereas large d promotes thermal relaxation.

Mechanistic interpretation

Each surface point experiences 70–260 overlapping pulses separated by approximately 2 μm, producing cyclic heating with $\Delta T \approx$ 400–600 K. The thermal-expansion mismatch between SiO_2 and Si ($\Delta\alpha \approx (2.5–3.5){\cdot}10^{-6}$ K^{-1}) induces in-plane compressive stress

$$\sigma = \frac{E_f \Delta\alpha \Delta T}{1 - \nu_f}. \qquad (3)$$

For the thermal-expansion mismatch between SiO_2 and Si and the measured temperature rise (ΔT), the resulting biaxial stress in the oxide film is only $\sigma_{mismitch} \approx$ 0.10–0.18 GPa, using E_f = 70 GPa and ν_f = 0.17 (Poisson's Ratio of SiO_2). This stress level alone is insufficient to reach the critical delamination threshold ($\sigma_c \approx$ 0.5–1.0 GPa for Γ_{int} = 0.3–0.8 J·m^{-2}), Eq. (3). The observed

Table 5. Experimental thresholds vs theoretical predictions

Transition	Experimental	Theoretical / Derived	Ref.
Wrinkle onset	$I \approx 1.4{\times}10^4$ W·cm^{-2} (at d = 519 μm)	Critical compressive stress $\sigma_c \approx$ 0.1–0.9 GPa (onset of elastic buckling)	[20, 22]
Blister onset	$I_{nuc} \approx 4{\times}10^4$ W·cm^{-2} (at d = 333 μm)	From Eq. (1): $\frac{\sigma_c^2 h}{2E_f} = \Gamma_{int} \approx 1.5$ J·m^{-2} → $\sigma_c \approx 0.9$ GPa	[9, 23]
Premelting	$I > 1{\times}10^5$ W·cm^{-2}	$T \approx 1700$ K (softening of SiO_2/Si interface)	[15, 25]
Si melting	$I > 2{\times}10^5$ W·cm^{-2}	T_m = 1687 K	[26]

blistering therefore results from cumulative multi-pulse effects: residual compressive stress from oxide growth, cyclic ratcheting over 70–260 pulses per point, and local adhesion weakening assisted by gas desorption and interfacial pressure. These combined factors raise the effective compressive stress above the classical single-pulse mismatch value, enabling interfacial delamination without requiring unrealistically high ΔT (> 2000 K). When this stress exceeds the elastic limit, wrinkles form; progressive heating and interfacial gas release (O_2, H_2O desorption) weaken adhesion, leading to blisters; at higher intensities, premelting disrupts both oxide and interface integrity. This hierarchy of thermo-mechanical instabilities — buckling, delamination, and melting — captures the dynamic interplay of optical, thermal, and mechanical effects in nanosecond scanning. The results extend classical static-buckling and fracture theories [23, 24] to the dynamic regime of cyclic nanosecond heating, quantitatively connecting process parameters to stress evolution.

Conclusions

This study establishes a quantitative and physically interpretable framework for laser-induced interfacial instabilities in oxide–semiconductor bilayers. By systematically varying the laser defocus, it is demonstrated that the coupled parameters of peak power density I and laser spot diameter d govern a continuous morphological transition from elastic wrinkling to interfacial blistering and ultimately premelting. The resulting defocus–intensity phase diagram represents the first statistically bounded process window linking measurable laser parameters to mechanical instability modes. Control experiments on stationary irradiation and bare silicon unequivocally prove that dynamic scanning and the oxide cap are both indispensable: without either, stresses relax via substrate slip rather than interfacial deformation. Chemical validation through Hydrofluoric etching further confirms that the intermediate blister morphology arises from true oxide delamination, not melting or oxidation.

Beyond its phenomenology, this work advances the fundamental understanding of rapid thermo-mechanical coupling in thin films, extending classical static-buckling and delamination theory into the nanosecond cyclic-heating regime. Defocus is identified as a continuous and universal control parameter, bridging optical process tuning with thin-film mechanics. The quantitative framework developed here provides not only a robust physical explanation for prior qualitative reports, but also a predictive guideline for precision, sub-melting laser surface engineering across dielectric–semiconductor systems.

References

1. Otobe T., Gushiken E. Influence of point defects on laser-induced excitation in silicon. *Physical Review Applied*, 2024, vol. 22, no. 6, pp. 064096. https://doi.org/10.1103/physrevapplied.22.064096
2. Kim W.J., Park K.-R., Ryu S.O., Kim B.S., Kwon J., Kim W.-B. Fundamental origin of Si surface defects caused by laser irradiation and prevention of suboxide formation through high density ultrathin SiO_2. *Applied Surface Science*, 2024, vol. 662, pp. 159997. https://doi.org/10.1016/j.apsusc.2024.159997
3. Zhou J.K., Su X.L., Zhang B.K., Zeng Y.H., Liu W., Ye J.C., et al. Ultrafast laser-annealing of hydrogenated amorphous silicon in tunnel oxide passivated contacts for high-efficiency n-type silicon solar cells. *Materials Today Energy*, 2024, vol. 42, pp. 101559. https://doi.org/10.1016/j.mtener.2024.101559
4. Bonse J., Höhm S., Kirner S.V., Rosenfeld A., Krüger J. Laser-induced periodic surface structures — a scientific evergreen. *IEEE Journal of Selected Topics in Quantum Electronics*, 2017, vol. 23, no. 3, pp. 9000615. https://doi.org/10.1109/JSTQE.2016.2614183
5. Namdari N., Mohammadian B., Jafari P., Mohammadi R., Sojoudi H., Ghasemi H., Rizvi R. Advanced functional surfaces through controlled damage and instabilities. *Materials Horizons*, 2020, vol. 7, no. 2, pp. 366–396. https://doi.org/10.1039/C9MH01516G
6. Wu Y., Xiang X., Yu J., Yuan X., Shen H., Zheng W., Zu X. Review: Research progress on nanosecond laser irradiation damage of optical films. *Nuclear Analysis*, 2022, vol. 1, no. 4, pp. 100045. https://doi.org/10.1016/j.nucana.2022.100045
7. Grigoriev F.V., Sulimov V.B., Tikhonravov A.V. Laser-induced thermal stresses in dense and porous Silicon Dioxide films. *Coatings*, 2021, vol. 11, no. 4, pp. 394. https://doi.org/10.3390/coatings11040394
8. Flores-Johnson E.A., Shen L., Annabattula R.K., Onck P.R., Shen Y.G., Chen Z. The effect of interface adhesion on buckling and cracking of hard thin films. *Applied Physics Letters*, 2014, vol. 105, no. 16, pp. 161912. https://doi.org/10.1063/1.4900443
9. McDonald J.P., Mistry V.R., Ray K.E., Yalisove S.M., Nees J.A., Moody N.R. Femtosecond-laser-induced delamination and blister formation in thermal oxide films on silicon (100). *Applied Physics Letters*, 2006, vol. 88, no. 15, pp. 153121, https://doi.org/10.1063/1.2193777

Литература

1. Otobe T., Gushiken E. Influence of point defects on laser-induced excitation in silicon // Physical Review Applied. 2024. V. 22. N 6. P. 064096. https://doi.org/10.1103/physrevapplied.22.064096
2. Kim W.J., Park K.-R., Ryu S.O., Kim B.S., Kwon J., Kim W.-B. Fundamental origin of Si surface defects caused by laser irradiation and prevention of suboxide formation through high density ultrathin SiO_2 // Applied Surface Science. 2024. V. 662. P. 159997. https://doi.org/10.1016/j.apsusc.2024.159997
3. Zhou J.K., Su X.L., Zhang B.K., Zeng Y.H., Liu W., Ye J.C., et al. Ultrafast laser-annealing of hydrogenated amorphous silicon in tunnel oxide passivated contacts for high-efficiency n-type silicon solar cells // Materials Today Energy. 2024. V. 42. P. 101559. https://doi.org/10.1016/j.mtener.2024.101559
4. Bonse J., Höhm S., Kirner S.V., Rosenfeld A., Krüger J. Laser-induced periodic surface structures — a scientific evergreen // IEEE Journal of Selected Topics in Quantum Electronics. 2017. V. 23. N 3. P. 9000615. https://doi.org/10.1109/JSTQE.2016.2614183
5. Namdari N., Mohammadian B., Jafari P., Mohammadi R., Sojoudi H., Ghasemi H., Rizvi R. Advanced functional surfaces through controlled damage and instabilities // Materials Horizons. 2020. V. 7. N. 2. P. 366–396. https://doi.org/10.1039/C9MH01516G
6. Wu Y., Xiang X., Yu J., Yuan X., Shen H., Zheng W., Zu X. Review: Research progress on nanosecond laser irradiation damage of optical films // Nuclear Analysis. 2022. V. 1. N 4. P. 100045. https://doi.org/10.1016/j.nucana.2022.100045
7. Grigoriev F.V., Sulimov V.B., Tikhonravov A.V. Laser-induced thermal stresses in dense and porous Silicon Dioxide films // Coatings. 2021. V. 11. N 4. P. 394. https://doi.org/10.3390/coatings11040394
8. Flores-Johnson E.A., Shen L., Annabattula R.K., Onck P.R., Shen Y.G., Chen Z. The effect of interface adhesion on buckling and cracking of hard thin films // Applied Physics Letters. 2014. V. 105. N 16. P. 161912. https://doi.org/10.1063/1.4900443
9. McDonald J.P., Mistry V.R., Ray K.E., Yalisove S.M., Nees J.A., Moody N.R. Femtosecond-laser-induced delamination and blister formation in thermal oxide films on silicon (100) // Applied Physics Letters. 2006. V. 88. N 15. P. 153121, https://doi.org/10.1063/1.2193777

10. Tsibidis G.D., Stratakis E., Aifantis K.E. Thermoplastic deformation of silicon surfaces induced by ultrashort pulsed lasers in submelting conditions. *Journal of Applied Physics*, 2012, vol. 111, no. 5, pp. 053502. https://doi.org/10.1063/1.3688020
11. Sopeña P., Wang A., Mouskeftaras A., Grojo D. Transmission laser welding of similar and dissimilar semiconductor materials. *Laser and Photonics Reviews*, 2022, vol. 16, no. 11, pp. 2200208. https://doi.org/10.1002/lpor.202200208
12. Huang C., Luo Z.A., Zhou H.Y., Yang J.S., Zhang Z.C., Fan M.R., et al. Effect of laser defocus on microstructural and mechanical properties of 316L stainless steel manufactured by laser powder bed fusion. *Journal of Materials Research and Technology*, 2025, vol. 38, pp. 3114–3130. https://doi.org/10.1016/j.jmrt.2025.08.099
13. Zhurba D.V., Zhurba V.M., Veiko V.P., Pankin D.V., Zhukov M.V., Puisha A.E. Investigation of phase transformations of carbon steel scale during laser purification by nanosecond pulses in the evaporation mode. *Scientific and Technical Journal of Information Technologies, Mechanics and Optics*, 2025, vol. 25, no. 2, pp. 179–189. (in Russian). https://doi.org/10.17586/2226-1494-2025-25-2-179-189
14. Matei A.T., Visan A.I., Negut I. Laser-fabricated micro/nanostructures: mechanisms, fabrication techniques, and applications. *Micromachines*, 2025, vol. 16, no. 5, pp. 573. https://doi.org/10.3390/mi16050573
15. Martan J., Cibulka O., Semmar N. Nanosecond pulse laser melting investigation by IR radiometry and reflection-based methods. *Applied Surface Science*, 2006, vol. 253, no. 3, pp. 1170–1177. https://doi.org/10.1016/j.apsusc.2006.01.077
16. Skvortsov A.M., Huynh Cong Tu, Khaletsky R. Mechanism of microstructuring in the SiO_2/Si system under scanning pulsed fiber laser irradiation. *Scientific and Technical Journal of Information Technologies, Mechanics and Optics*, 2013, no. 3 (85), pp. 137–143. (in Russian)
17. Otsu N. A threshold selection method from gray-level histograms. *IEEE Transactions on Systems, Man, and Cybernetics*, 1979, vol. 9, no. 1, pp. 62–66. https://doi.org/10.1109/tsmc.1979.4310076
18. Born M., Wolf E. *Principles of Optics: Electromagnetic Theory of Propagation, Interference and Diffraction of Light*. Cambridge University Press, 1999, 985 p.
19. Sasaki S., Izumi T., Hara T. Delamination of Si by high dose H-ion implantation through thin SiO_2 film (ESR characterization). *Materials Science and Engineering: B*, 2002, vol. 91-92, pp. 160–163. https://doi.org/10.1016/s0921-5107(01)00984-9
20. Song J., Jiang H., Liu Z.J., Khang D.Y., Huang Y., Rogers J.A., et al. Buckling of a stiff thin film on a compliant substrate in large deformation. *International Journal of Solids and Structures*, 2008, vol. 45, no. 10, pp. 3107–3121. https://doi.org/10.1016/j.ijsolstr.2008.01.023
21. Sakurai H., Konishi K., Tamaru H., Yumoto J., Kuwata-Gonokami M. Direct correlation of local fluence to single-pulse ultrashort laser ablated morphology. *Communications Materials*, 2021, vol. 2, no. 1, p. 38. https://doi.org/10.1038/s43246-021-00138-x
22. Velli M.-C., Tsibidis G.D., Mimidis A., Skoulas E., Pantazis Y., Stratakis E. Predictive modeling approaches in laser-based material processing. *Journal of Applied Physics*, 2020, vol. 128, no. 18, p. 183102. https://doi.org/10.1063/5.0018235
23. De Baere D., Van Cauwenbergh P., Bayat M., Mohanty S., Thorborg J., Thijs L., et al. Thermo-mechanical modelling of stress relief heat treatments after laser-based powder bed fusion. *Additive Manufacturing*, 2021, vol. 38, pp. 101818. https://doi.org/10.1016/j.addma.2020.101818
24. Yu H.-H., Hutchinson J.W. Influence of substrate compliance on buckling delamination of thin films. *International Journal of Fracture*, 2002, vol. 113, no. 1, pp. 39–55. https://doi.org/10.1023/A:1013790232359
25. Son Y.-I., Shin J. Numerical study on the laser annealing of silicon used in advanced V-NAND device. *Materials*, 2022, vol. 15, no. 12, pp. 4201. https://doi.org/10.3390/ma15124201
26. Kan Z., Zhu Q., Ren H., Shen M. Femtosecond laser-induced thermal transport in silicon with liquid cooling bath. *Materials*, 2019. vol. 12, no. 13, pp. 2043. https://doi.org/10.3390/ma12132043

10. Tsibidis G.D., Stratakis E., Aifantis K.E. Thermoplastic deformation of silicon surfaces induced by ultrashort pulsed lasers in submelting conditions // Journal of Applied Physics. 2012. V. 111. N 5. P. 053502. https://doi.org/10.1063/1.3688020
11. Sopeña P., Wang A., Mouskeftaras A., Grojo D. Transmission laser welding of similar and dissimilar semiconductor materials // Laser and Photonics Reviews. 2022. V. 16. N 11. P. 2200208. https://doi.org/10.1002/lpor.202200208
12. Huang C., Luo Z.A., Zhou H.Y., Yang J.S., Zhang Z.C., Fan M.R., et al. Effect of laser defocus on microstructural and mechanical properties of 316L stainless steel manufactured by laser powder bed fusion // Journal of Materials Research and Technology. 2025. V. 38. P. 3114–3130. https://doi.org/10.1016/j.jmrt.2025.08.099
13. Журба Д.В., Журба В.М., Вейко В.П., Панькин Д.В., Жуков М.В., Пуйша А.Э. Исследование фазовых превращений окалины углеродистой стали при лазерной очистке наносекундными импульсами в режиме испарения // Научно-технический вестник информационных технологий, механики и оптики. 2025. Т 25. № 2. С. 179–189. https://doi.org/10.17586/2226-1494-2025-25-2-179-189
14. Matei A.T., Visan A.I., Negut I. Laser-fabricated micro/nanostructures: mechanisms, fabrication techniques, and applications // Micromachines. 2025. V. 16. N 5. P. 573. https://doi.org/10.3390/mi16050573
15. Martan J., Cibulka O., Semmar N. Nanosecond pulse laser melting investigation by IR radiometry and reflection-based methods // Applied Surface Science. 2006. V. 253. N 3. P. 1170–1177. https://doi.org/10.1016/j.apsusc.2006.01.077
16. Скворцов А.М., Хуинь Конг Ту, Халецкий Р.А. Механизм микроструктурирования системы SiO_2/Si при облучении сканирующим пучком импульсного волоконного лазера // Научно-технический вестник информационных технологий, механики и оптики. 2013. № 3 (85). С. 137–143.
17. Otsu N. A threshold selection method from gray-level histograms // IEEE Transactions on Systems, Man, and Cybernetics. 1979. V. 9. N 1. P. 62–66. https://doi.org/10.1109/tsmc.1979.4310076
18. Born M., Wolf E. Principles of Optics: Electromagnetic Theory of Propagation, Interference and Diffraction of Light. Cambridge University Press, 1999. 985 p.
19. Sasaki S., Izumi T., Hara T. Delamination of Si by high dose H-ion implantation through thin SiO_2 film (ESR characterization) // Materials Science and Engineering: B. 2002. V. 91-92. P. 160–163. https://doi.org/10.1016/s0921-5107(01)00984-9
20. Song J., Jiang H., Liu Z.J., Khang D.Y., Huang Y., Rogers J.A., et al. Buckling of a stiff thin film on a compliant substrate in large deformation // International Journal of Solids and Structures. 2008. V. 45. N 10. P. 3107–3121. https://doi.org/10.1016/j.ijsolstr.2008.01.023
21. Sakurai H., Konishi K., Tamaru H., Yumoto J., Kuwata-Gonokami M. Direct correlation of local fluence to single-pulse ultrashort laser ablated morphology // Communications Materials. 2021. V. 2. N 1. P. 38. https://doi.org/10.1038/s43246-021-00138-x
22. Velli M.-C., Tsibidis G.D., Mimidis A., Skoulas E., Pantazis Y., Stratakis E. Predictive modeling approaches in laser-based material processing // Journal of Applied Physics. 2020. V. 128. N 18. P. 183102. https://doi.org/10.1063/5.0018235
23. De Baere D., Van Cauwenbergh P., Bayat M., Mohanty S., Thorborg J., Thijs L., et al. Thermo-mechanical modelling of stress relief heat treatments after laser-based powder bed fusion // Additive Manufacturing. 2021. V. 38. P. 101818. https://doi.org/10.1016/j.addma.2020.101818
24. Yu H.-H., Hutchinson J.W. Influence of substrate compliance on buckling delamination of thin films // International Journal of Fracture. 2002. V. 113. N 1. P. 39–55. https://doi.org/10.1023/A:1013790232359
25. Son Y.-I., Shin J. Numerical study on the laser annealing of silicon used in advanced V-NAND device // Materials. 2022. V. 15. N 12. P. 4201. https://doi.org/10.3390/ma15124201
26. Kan Z., Zhu Q., Ren H., Shen M. Femtosecond laser-induced thermal transport in silicon with liquid cooling bath // Materials. 2019. V. 12. N 13. P. 2043. https://doi.org/10.3390/ma12132043

Author

Huynh Cong Tu — PhD, Lecturer, Deputy Head of Academic Affairs Office, Quy Nhon University, Quy Nhon, 55131, Viet Nam, https://orcid.org/0000-0002-5184-8242, huynhcongtu@qnu.edu.vn

Автор

Хуинь Конг Ту — PhD, преподаватель, заместитель начальника учебного управления, Университет Куинён, Куинён, 55131, Вьетнам, https://orcid.org/0000-0002-5184-8242, huynhcongtu@qnu.edu.vn

Received 18.09.2025
Approved after reviewing 08.11.2025
Accepted 22.01.2026

Статья поступила в редакцию 18.09.2025
Одобрена после рецензирования 08.11.2025
Принята к печати 22.01.2026